

Unveiling a multi-component stochastic gravitational-wave background with the TianQin + LISA network

Zheng-Cheng Liang,¹ Zhi-Yuan Li,² En-Kun Li,² Jian-dong Zhang,² and Yi-Ming Hu^{2,*}

¹*School of Physics, Henan Normal University, Xinxiang 453007, China*

²*MOE Key Laboratory of TianQin Mission, TianQin Research Center for Gravitational Physics & School of Physics and Astronomy, Frontiers Science Center for TianQin, CNSA Research Center for Gravitational Waves, Sun Yat-sen University (Zhuhai Campus), Zhuhai 519082, China*

(Dated: February 18, 2025)

Space-borne detectors, including TianQin and Laser Interferometry Space Antenna (LISA), are tasked with simultaneously observing the Galactic foreground, astrophysical and cosmological stochastic gravitational-wave backgrounds (SGWBs). For the first time, we employ a space-borne detector network to identify these SGWBs. Specifically, we develop a tailored likelihood for cross-correlation detection with such networks. Combined with the likelihood, we use the simulated datasets of the TianQin + LISA network to conduct an analysis for model selection and parameter estimation. In our analysis, we adopt an astrophysical background originating from extragalactic white-dwarf binaries, along with a flat cosmological background associated with the early Universe. Our results indicate that, after 4 years of operation, the network could detect a single SGWB from either astrophysical or cosmological origins, with an energy density $\Omega_{\text{ast/cos}}$ (10 mHz) on the order of 10^{-12} , despite the presence of a Galactic foreground. Furthermore, to distinguish the cosmological background from both a Galactic foreground and an extragalactic background produced by white-dwarf binaries, the energy density Ω_{cos} should reach around 2×10^{-11} .

I. INTRODUCTION

The stochastic gravitational-wave (GW) background (SGWB) is formed by numerous GW sources, each insufficiently strong to be resolvable by detectors. The background can be categorized into two main domains: astrophysical- and cosmological-origin. The astrophysical SGWB is primarily sourced from compact binaries, offering a glimpse into the structure of our galaxy and the history of galaxy mergers [1–3]. The cosmological SGWB stems from early Universe processes, bearing primordial information of the early Universe [4–10].

Given the challenge of distinguishing SGWB from detector noise, cross-correlation method [11–18] and null-channel method [19–22] have been proposed. For terrestrial detectors such as ground-based detectors and Pulsar Timing Arrayss (PTAs), cross-correlating data from two detectors can distinguish the SGWB signal from the detector noise, based on the assumption that the noise in the two detectors is uncorrelated. Ground-based detectors have made strides by setting upper limits on the dimensionless energy parameter Ω_{gw} within the frequency range of hundreds of Hertz [17, 23–29]. Concurrently, PTA collaborations have reported the presence of an SGWB in the nano-Hertz (nHz) band, marking significant progress in the SGWB detection [30–33]. An alternative method can be employed for future space-borne detectors, such as TianQin and the Laser Interferometry Space Antenna (LISA), which operate in the milli-Hertz (mHz) band. Typically arranged in triangular formations, these detectors can establish signal-insensitive

data from a null channel. The null channel is capable of monitoring the detector noise. Consequently, the SGWB signal can be extracted by auto-correlating the data from the detector [34–48].

GW detectors anticipate encountering a complex blend of SGWB originating from diverse sources. To extract information regarding the diverse origins from the SGWB, it is essential to conduct component separation [49–62]. For space-borne detectors, a predominant foreground is anticipated to arise from unresolved Galactic double white dwarfs (DWDs), potentially masking the detection of SGWBs from other sources [63–73]. A single LISA can offer the capability to separate backgrounds generated by nearby dwarf galaxies [74] or cosmological sources [35, 36, 38, 41, 75] from the Galactic foreground. Additionally, it can promote further discrimination between astrophysical and cosmological origins [76]. Nevertheless, the null-channel method employed in single detectors is susceptible to uncertainties in detector noise characterization. Such uncertainties can compromise the precision of constraining stochastic backgrounds, potentially leading to a degradation in accuracy by 1-2 orders of magnitude [46]. The cross-correlation method, which harnesses the synergy of multiple space-borne detectors, is crucial to overcome these limitations.

In this paper, we utilize the cross-correlation between space-borne detectors to separate the components of SGWB, adopting a Bayesian strategy that is implemented by a sampling algorithm [77–80]. Recognizing the concurrent operational periods and shared detection frequency bands of TianQin [81] and LISA [82], we leverage the TianQin + LISA (TL) network. Accounting for the response and noise budget of TianQin and LISA, we formulate a robust likelihood function, which is designed to handle SGWBs of arbitrary

* huyiming@sysu.edu.cn

intensities and incorporates data folding to enhance processing efficiency [83, 84]. Additionally, we synthesize detector noise, Galactic foreground, extragalactic background, and cosmological background to generate simulated datasets. By applying the likelihood function to conduct Bayesian inference on the simulated datasets, our analysis is twofold: we gauge the network's effectiveness in differentiating between Galactic foreground, astrophysical and cosmological SGWBs through model selection; and we evaluate the TL network's ability to constrain SGWB parameters in the presence of a Galactic foreground via parameter estimation.

The structure of this paper is as follows. Sec. II provides an overview of the essential quantities in SGWB detection. Building on this foundation, Sec. III introduces the methodology for cross-correlation detection. The setup of analysis is laid out in Sec. IV. Sec. V delves into the model selection and parameter estimation for SGWBs. Finally, Sec. VI presents the conclusion, comparison of studies, and discussion regarding future extensions.

II. KEY QUANTITIES FOR DETECTION

An SGWB originates from a large number of unresolved GW events, collectively resembling detector noise¹. This background cannot be fully understood through isolated events, but rather requires statistical analysis. One way to characterize SGWB is by examining the expectation values of field variables, which includes analyzing the Fourier components of metric perturbations when expanded into plane waves. In this section, we will delve into the essential quantities for SGWB detection, particularly emphasizing the statistical properties of both the SGWB signal and the detector noise.

A. Statistical properties of stochastic background

In transverse-traceless gauges, the metric perturbations $h(t, \vec{x})$ associated with an SGWB can be represented as a superposition of sinusoidal plane waves, which propagate in various directions \hat{k} and at different frequencies f [85]:

$$h(t, \vec{x}) = \sum_P \int_{-\infty}^{\infty} df \int_{S^2} d\hat{\Omega}_{\hat{k}} \tilde{h}_P(f, \hat{k}) \mathbf{e}^P(\hat{k}) e^{i2\pi f[t - \hat{k} \cdot \vec{x}(t)/c]} \quad (1)$$

Here, \vec{x} represents the location where the GW measurement is conducted at time t , with c signifying the speed of light. The spin-2 polarization basis tensor \mathbf{e}^P corresponds to the two independent polarizations $P = +, \times$ of

¹ In many aspects, such as the spectral shape, Gaussianity, stationarity, and anisotropy, the SGWB is not noise-like.

GWs. The Fourier amplitude \tilde{h}_P captures the frequency-domain characteristics of GWs for each given propagation direction.

The statistical properties of an SGWB can be characterized by the moments of its Fourier amplitude. For the most straightforward case, where the SGWB is Gaussian-stationary, unpolarized, and isotropic, the statistical properties can be defined as follows:

$$\langle \tilde{h}_P(f, \hat{k}) \rangle = 0, \quad (2)$$

$$\langle \tilde{h}_P(f, \hat{k}) \tilde{h}_{P'}^*(f', \hat{k}') \rangle = \frac{1}{16\pi} \delta(f - f') \delta_{PP'} \delta^2(\hat{k}, \hat{k}') S_h(|f|), \quad (3)$$

where $\langle \dots \rangle$ represents the ensemble average, δ and δ_{ij} denote the Dirac delta function and Kronecker symbol, respectively. To ensure that S_h is understood as a one-sided power spectral density (PSD):

$$S_h(f) = \lim_{T \rightarrow \infty} \frac{1}{T} \left\langle \left| \int_{-T/2}^{T/2} dt h(t) e^{-i2\pi f t} \right|^2 \right\rangle, \quad (4)$$

which involves both polarizations and integrates over the entire sky, a prefactor of $1/16\pi$ has been included.

Alongside the PSD S_h , the dimensionless energy spectrum density Ω_{gw} is another essential metric, which exhibits a direct relationship with S_h [86, 87]:

$$\Omega_{\text{gw}}(f) = \frac{1}{\rho_c} \frac{d\rho_{\text{gw}}}{d(\ln f)} = \frac{2\pi^2}{3H_0^2} f^3 S_h(f). \quad (5)$$

Here, ρ_{gw} denotes the GW energy density. The critical energy density is defined as $\rho_c = 3H_0^2 c^2 / (8\pi G)$, where G is the gravitational constant and H_0 is the Hubble constant.

In this paper, we examine the energy spectrum density, which can be categorized into three distinct forms. The first one arises from the Galactic foreground. The corresponding PSD is given by the polynomial expression [88]:

$$S_h(f) = \frac{20}{3} \left[10^{\sum_i a_i x^i(f)} \right]^2, \quad (6)$$

where the factor of $20/3$ is related to the response of space-borne detectors to GWs for the all-sky average [70, 89], and the function $x(f) = \log(f/10^{-3} \text{ Hz})$ is defined with polynomial coefficients a_i . Note that the PSD of the Galactic foreground is associated with the observation time of detectors, which we will address in Sec. IV B. The second one pertains to the astrophysical SGWB. Its energy spectrum density is characterized by a power-law form:

$$\Omega_{\text{gw}}(f) = \Omega_{\text{ast}} \left(\frac{f}{f_{\text{ref}}} \right)^{\alpha_{\text{ast}}}, \quad (7)$$

where the spectral index α_{ast} can be set to $2/3$ for a binary coalescence within the mHz band [90], and the reference frequency f_{ref} is chosen to be arbitrary. Lastly, the cosmological SGWB is predicted to have a nearly flat spectrum [91–93]:

$$\Omega_{\text{gw}}(f) = \Omega_{\text{cos}}. \quad (8)$$

B. Signal and noise PSDs

Space-borne GW detectors, such as TianQin and the LISA, are specifically designed to detect GWs in the mHz band. TianQin will feature an equilateral triangle configuration, with three identical satellites orbiting Earth at an arm length of approximately 1.7×10^5 km. It will have an orbital period of 3.64 days and will operate on a schedule alternating between “three months on” and “three months off” [94]. LISA also utilizes a triangular configuration, but it will orbit the Sun, trailing behind the Earth by about 20° . The three satellites in LISA will maintain a separation of roughly 2×10^6 km from one another. LISA’s orbital period is synchronized with that of the Earth, completing one orbit around the Sun within a year. It is important to note that while TianQin and LISA can potentially form the TL network for GW detection, their joint observation time is limited to only half of their operation time due to TianQin’s working mode. This constraint will be generally applied throughout the analysis of this paper.

The SGWB signal in a detector channel I can be represented as the convolution of channel response $\mathbb{F}_I(t, \vec{x})$ and metric perturbations $h(t, \vec{x})$ [95]. Given the detector motion, which introduces variations in the response, it is advantageous to focus on a narrow time interval, defined as $[\tau - T/2, \tau + T/2]$, to ensure that the GW measurement location and the channel response are nearly static. Consequently, the SGWB signal can be expressed as:

$$\begin{aligned} h_I(t, \tau) &= \mathbb{F}_I[t, \vec{x}_I(\tau)] * h[t, \vec{x}_I(\tau)] \\ &= \int_{-\infty}^{\infty} df \sum_P \int_{S^2} d\hat{\Omega}_{\hat{k}} F_I^P(f, \hat{k}, \tau) \tilde{h}_P(f, \hat{k}) \\ &\quad \times e^{i2\pi f[t - \hat{k} \cdot \vec{x}_I(\tau)/c]}, \end{aligned} \quad (9)$$

where τ is employed to label the specific time interval, the frequency-domain response F_I^P is determined by the polarization tensor and the detector channel I [89]. Within this framework, the PSD and cross-spectral density of the frequency-domain signal $\tilde{h}_{I,J}$ are determined by

$$\langle \tilde{h}_I(f, \tau) \tilde{h}_J^*(f', \tau) \rangle = \frac{1}{2} \delta(f - f') \Gamma_{IJ}(f, \tau) S_h(|f|), \quad (10)$$

where the overlap reduction function (ORF) involves both the channel response F_I^P and the separation vector $\Delta\vec{x} = \vec{x}_I - \vec{x}_J$ between channels² [96]:

$$\begin{aligned} \Gamma_{IJ}(f, \tau) &= \frac{1}{8\pi} \sum_P \int_{S^2} d\hat{\Omega}_{\hat{k}} F_I^P(f, \hat{k}, \tau) F_J^{P*}(f, \hat{k}, \tau) \\ &\quad \times e^{-i2\pi f \hat{k} \cdot \Delta\vec{x}(\tau)/c}. \end{aligned} \quad (11)$$

In the SGWB detection, it is imperative to account for not only the signal itself but also the detector noise. For

space-borne detectors, the inherent motion introduces uncancelable phase noise. It is necessary to use the time delay interferometry (TDI) techniques to suppress the phase noise by several orders of magnitude, ensuring that the phase noise is lower than the target GW level [97, 98]. Among the various TDI combinations, the unequal-arm Michelson (X, Y, Z) involves the measurements of neighboring links for each satellite. Building upon the (X, Y, Z) setup, a more advanced setup referred to as the noise-orthogonal unequal-arm Michelson (A, E, T) can be constructed, according to Ref. [99], as follows³:

$$\begin{aligned} A &= \frac{1}{\sqrt{2}}(Z - X), \\ E &= \frac{1}{\sqrt{6}}(X - 2Y + Z), \\ T &= \frac{1}{\sqrt{3}}(X + Y + Z). \end{aligned} \quad (12)$$

Assuming that the noise is stationary, the noise PSD for the (A, E, T) setup is given by

$$\begin{aligned} P_{n_{A/E}}(f) &= \frac{2 \sin^2 u}{L^2} \left[(\cos u + 2) S_p(f) \right. \\ &\quad \left. + 2(\cos(2u) + 2\cos u + 3) \frac{S_a(f)}{(2\pi f)^4} \right], \\ P_{n_T}(f) &= \frac{8 \sin^2 u \sin^2 \frac{u}{2}}{L^2} \left[S_p(f) + 4 \sin^2 \frac{u}{2} \frac{S_a(f)}{(2\pi f)^4} \right], \end{aligned} \quad (13)$$

where $u = (2\pi f L)/c$ is determined by the detector arm length L , S_p and S_a denote the PSDs of optical-metrology system noise and acceleration noise, respectively. For more comprehensive details about the parameters of TianQin and LISA, readers are recommended to refer to Refs. [100, 101]. Unless otherwise stated, our study primarily focuses on the case using the (A, E, T) setup.

III. METHODOLOGY

Statistical inference is a powerful tool for identifying the presence of an SGWB signal within observation data. This process is commonly pursued through both classical (frequentist) and Bayesian inference methodologies. In this section, we constrain our focus on parameter estimation and model selection in the context of SGWB detection, opting for a Bayesian inference approach.

² For space-borne detectors, a satellite can be selected as the reference location of the channel.

³ In this paper, we assume a completely equilateral configuration; otherwise, the AET channels will not be noise-orthogonal [45].

A. Bayesian inference

Bayesian inference offers a robust quantitative framework for gauging the uncertainties associated with unknown parameters. This estimation process hinges on the posterior probability distribution, which is formulated through the application of Bayes' theorem. Bayes' theorem updates the prior distribution $p(\boldsymbol{\theta})$ of the parameters $\boldsymbol{\theta}$ with the likelihood $p(d|\boldsymbol{\theta})$, thereby yielding the posterior distribution of the observations given the parameters:

$$p(\boldsymbol{\theta}|d) = \frac{p(d|\boldsymbol{\theta})p(\boldsymbol{\theta})}{p(d)}, \quad (14)$$

where the Bayesian evidence serves as a normalization factor:

$$p(d) = \int d\boldsymbol{\theta} p(d|\boldsymbol{\theta})p(\boldsymbol{\theta}). \quad (15)$$

The posterior distribution encodes the information from the data with our prior knowledge, providing a comprehensive estimation of the parameters.

Bayesian inference is not merely for parameter estimation; it also serves as a discerning tool for selecting a credible model or hypothesis from a collection of alternatives, each characterized by a set of parameters. In the subsequent discussion, we will denote the hypothesis as \mathcal{H}_a , where the subscript index a encompasses the range of competing hypotheses and the associated set of parameters as $\boldsymbol{\theta}_a$. Regarding Eq. (14), the joint posterior distribution for the parameters $\boldsymbol{\theta}_a$, conditioned on the \mathcal{H}_a , is expressed as

$$p(\boldsymbol{\theta}_a|d, \mathcal{H}_a) = \frac{p(d|\boldsymbol{\theta}_a, \mathcal{H}_a)p(\boldsymbol{\theta}_a|\mathcal{H}_a)}{p(d|\mathcal{H}_a)}. \quad (16)$$

In terms of the evidence $p(d|\mathcal{H}_a)$, the posterior probability for \mathcal{H}_a is provided by Bayes' theorem as follows:

$$p(\mathcal{H}_a|d) = \frac{p(d|\mathcal{H}_a)p(\mathcal{H}_a)}{P(d)}, \quad (17)$$

where $P(d)$ denotes the evidence across all the models considered. To compare the relative support \mathcal{H}_a and \mathcal{H}_b , the posterior odds ratio is computed:

$$\mathcal{O}_{ab}(d) = \frac{p(\mathcal{H}_a|d)}{p(\mathcal{H}_b|d)} = \frac{p(\mathcal{H}_a)}{p(\mathcal{H}_b)} \frac{p(d|\mathcal{H}_a)}{p(d|\mathcal{H}_b)}. \quad (18)$$

In the absence of a priori preferences favoring one hypothesis over the other, the prior probabilities $p(\mathcal{H}_a)$ and $p(\mathcal{H}_b)$ are assumed equal, reducing the odds ratio to the *Bayes factor*:

$$\mathcal{B}_{ab} = \frac{p(d|\mathcal{H}_a)}{p(d|\mathcal{H}_b)}. \quad (19)$$

The Bayes factor thus emerges as a critical metric for model selection. A positive log-Bayes factor, $\ln(\mathcal{B}_{ab})$, signifies that the data favors the hypothesis \mathcal{H}_a . It is conventional to interpret $\ln \mathcal{B}_{ab} > 1$ as an indication of positive evidence, a stronger level of support for the model

\mathcal{H}_a is acknowledged when $\ln \mathcal{B}_{ab} > 3$, and the support is considered very strong when $\ln \mathcal{B}_{ab} > 5$ [102].

Nested sampling [103] is an advanced technique used to provide samples of the posterior distribution, given a specified likelihood function and prior distribution [77–80]. The algorithm starts by randomly selecting a fixed number of live points from the prior distribution. In each iteration i , the live point with the lowest likelihood is replaced with a new point drawn from the prior region where the likelihood $p(d|\boldsymbol{\theta})$ exceeds p_i . The iterative process continues until a predefined termination criterion is met, yielding a collection of samples (referred to as dead points) along with any remaining live points. These points are then employed for both evidence calculation and parameter estimation, where the evidence can be utilized for model selection.

B. Likelihood for cross-correlation detection

The analysis presented above has indicated that the likelihood function is of critical importance for parameter estimation and model selection. Next, we turn our attention to derive the likelihood for the SGWB detection.

Given the constraints of the null-channel method for single detectors, which are significantly limited by uncertainties in noise knowledge [46], we propose a cross-correlation approach for SGWB detection using the TL network. However, the variability of the ORF for the TL network necessitates segmenting the data into manageable intervals. Each segment must be longer than the light-travel time between the detectors to ensure effective correlation, yet short enough to maintain the stability of the ORF throughout. For each segment, a Fourier transform over the designated time interval can be given by

$$\tilde{s}_I^i(f) = \int_{t_i-T/2}^{t_i+T/2} dt s_I(t) e^{-i2\pi f t}, \quad (20)$$

where i labels each time interval. By utilizing the Fourier transforms \tilde{s}_I^i , one can construct the following estimator for the S_h measured by detectors [104]:

$$\hat{C}_{IJ}^i(f) = \frac{2}{T} \frac{\tilde{s}_I^i(f) \tilde{s}_J^{i*}(f)}{\Gamma_{IJ}^i(f)}. \quad (21)$$

Assuming that the detector noise is Gaussian, stationary, the variance of the estimators is given by⁴

$$(\sigma_{IJ}^i(f))^2 \approx \frac{1}{2T\delta f} \frac{P_{s_I}(f)P_{s_J}(f)}{|\Gamma_{IJ}^i(f)|^2}, \quad (22)$$

⁴ While this formula applies to the SGWB of any intensity, it is crucial to emphasize that the ORF for cross-correlation between two detectors should be significantly less than that for auto-correlation within single detectors. The TL network, as noted in Ref. [88], adheres to this essential criterion.

where δf is the width of each frequency bin, the total PSD

$$P_{s_I}(f) = P_{n_I}(f) + \Gamma_{II}(f)S_h(f). \quad (23)$$

It is crucial to recognize that in the weak-signal limit, where the SGWB signal is significantly weaker than the detector noise, the total PSD can be attributed entirely to the detector noise. However, for space-borne detectors such as TianQin and LISA, the anticipated SGWB signal can surpass the detector noise. Consequently, the PSD as described in Eq. (23) should be amended to include the contribution of the SGWB signal.

For the TL network, cross-correlation can be effectively carried out using the four-channel pairs $\{\text{AA}', \text{AE}', \text{EA}', \text{EE}'\}$ [96, 105], where the prime symbol is used to differentiate between TianQin and LISA. Consequently, when the data is segmented into N parts, there are $4N \hat{C}_{IJ}$ to handle. To achieve an optimal expected signal-to-noise ratio (SNR) for SGWB detection, the numerous $\hat{C}_{IJ}(f)$ can be combined into a single estimator through a weighted sum [15, 106–108]:

$$\hat{C}_{\text{tot}}(f) = \frac{\sum_i \sum_{IJ} \hat{C}_{IJ}^i(f) (\sigma_{IJ}^i(f))^{-2}}{\sum_i \sum_{IJ} (\sigma_{IJ}^i(f))^{-2}}. \quad (24)$$

This construction process is analogous to data folding [83, 84], which helps in efficiently handling the data.

According to the construction, the weighted estimator is also applicable to the S_h :

$$\begin{aligned} \langle \hat{C}_{\text{tot}}(f) \rangle &= \frac{\langle \hat{C}_{IJ}^i(f) \rangle \sum_i \sum_{IJ} (\sigma_{IJ}^i(f))^{-2}}{\sum_i \sum_{IJ} (\sigma_{IJ}^i(f))^{-2}} \\ &= S_h(f), \end{aligned} \quad (25)$$

and the variances of the optimal estimator are added in the same way as electrical resistors in parallel to maximize SNR [15]:

$$\begin{aligned} \sigma_{\text{tot}}^2(f) &= \frac{1}{\sum_i \sum_{IJ} (\sigma_{IJ}^i(f))^{-2}} \\ &\approx \frac{1}{2T\delta f \sum_i \sum_{IJ} |\Gamma_{IJ}^i(f)|^2 / (P_{s_I}(f)P_{s_J}(f))} \\ &= \frac{1}{2T\delta f} \frac{P_{s_I}(f)P_{s_J}(f)}{N\bar{\Gamma}_{\text{tot}}^2(f)}, \end{aligned} \quad (26)$$

where it is assumed that the channels of the same detector share the same noise PSD, allowing for a more straightforward calculation of the total uncertainty in the cross-correlation. The time-averaged ORF is given by

$$\bar{\Gamma}_{\text{tot}}(f) = \sqrt{\frac{\sum_i \sum_{IJ} |\Gamma_{IJ}^i(f)|^2}{N}}. \quad (27)$$

In the context of measuring the specific $\hat{C}_{\text{tot}}(f)$ within a single frequency bin, the log-likelihood is expressed as

$$\ln [p(\hat{C}_{\text{tot}}(f)|\boldsymbol{\theta})] \propto -\frac{|\hat{C}_{\text{tot}}(f) - S_h(f, \boldsymbol{\theta})|^2}{2\sigma_{\text{tot}}^2(f)}, \quad (28)$$

where $\boldsymbol{\theta}$ denotes the model parameter of the SGWB, and the variance is provided by Eq. (26). For the entire frequency range, the full log-likelihood is the sum of individual log-likelihoods across each frequency bin:

$$\ln [\mathcal{L}(\boldsymbol{\theta})] = \mathcal{N} \sum_f \ln \left[p(\hat{C}_{\text{tot}}(f)|\boldsymbol{\theta}) \right], \quad (29)$$

where \mathcal{N} is a normalization factor.

IV. ANALYSIS SETUP

The full log-likelihood presented in Eq. (29) involves several critical aspects: the cross-correlation estimator \hat{C}_{tot} , the models of the SGWB intensity (S_h or Ω_{gw}), the priors of model parameters, and the corresponding statistical error σ_{tot} . Next, we will undertake a detailed examination of each of these elements, aiming to construct a clear and coherent narrative that elaborates the data processing pipeline for cross-correlation detection.

A. Segment duration

In the construction of the cross-correlation estimator, calculating the ORFs for each segment is essential. If the ORF does not change significantly within a segment, one can use the midpoint ORF value as a representative for the entire segment. Nonetheless, the effective ORF for this segment should be derived by dividing the ORF integral over that time period by the data duration T :

$$\Gamma_{IJ}^{\text{eff}}(f) = \frac{1}{T} \int_{-T/2}^{T/2} dt \Gamma_{IJ}(t, f). \quad (30)$$

This approximation can impact the accuracy and reliability of the subsequent Bayesian inference. Shorter segments inherently reduce the deviation, but practical considerations must be taken into account: to ensure the integrity of frequency-domain data and prevent the loss of information within the sensitive band of the detectors, it is crucial to select segments of sufficient duration. Both TianQin and LISA are sensitive within the mHz frequency band, necessitating the choice of at least an hourly segment duration.

Given the significantly shorter orbital period of TianQin compared to LISA, it can be approximated that LISA remains stationary while TianQin completes its 3.64-day orbital period. Moreover, given that the A/E channels can be effectively considered as two L-shaped interferometers with an offset angle of 45° [105], we can expect that the period of the ORF for $\{\text{AA}', \text{AE}', \text{EA}', \text{EE}'\}$ will be one-fourth (as TianQin rotates 90°) of that of TianQin, and we can choose the ORF for the AA' pair as a representative case. In Fig. 1, we present the absolute value of the relative error \mathcal{E}_r of the ORF $\Gamma_{\text{AA}'}^{\text{TL}}$ at 1

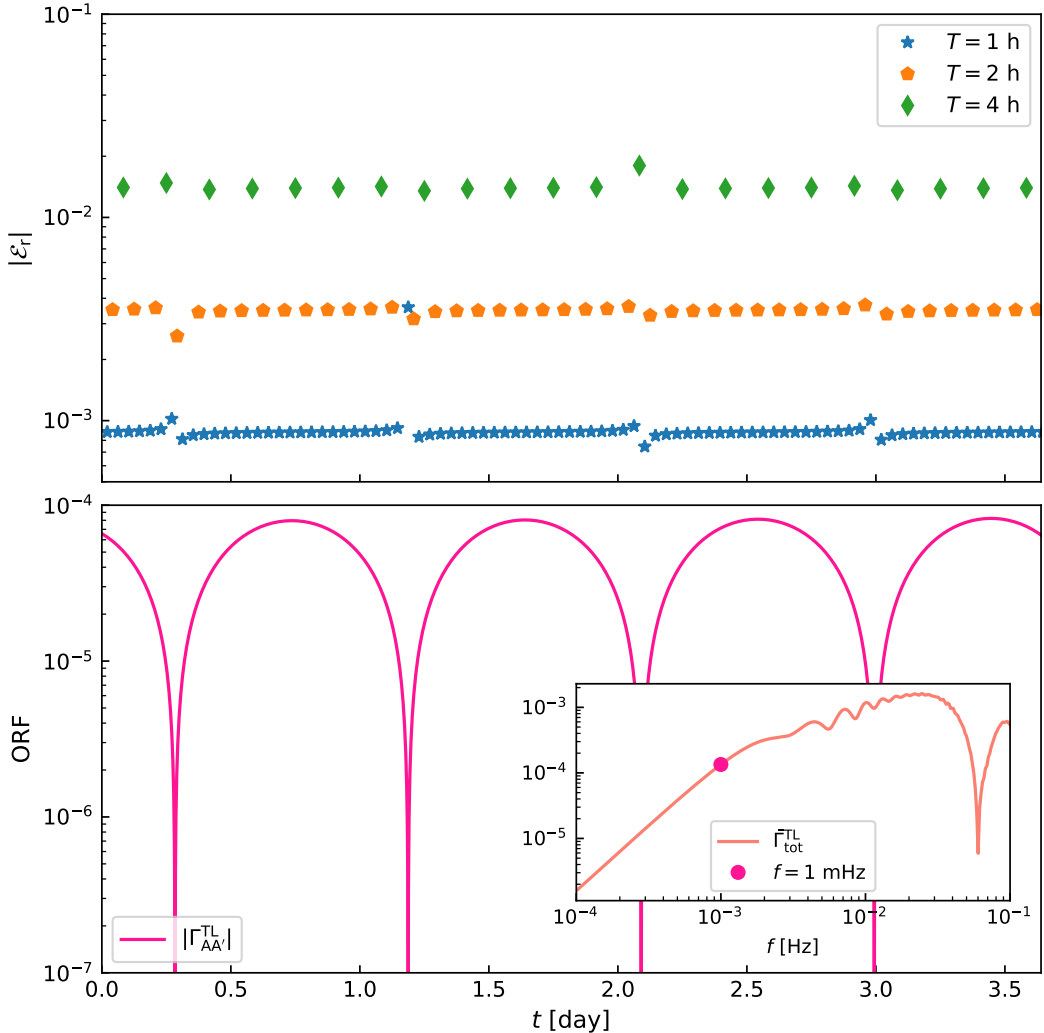


FIG. 1. Relative error of the ORF at 1 mHz. In the top panel, the points are color-coded to correspond to different segment lengths: blue, orange, and green dots denote 1 hour, 2 hours, and 4 hours, respectively. In the bottom panel, the results of the ORF are also included for reference, with the total ORF for $\{\text{AA}', \text{AE}', \text{EA}', \text{EE}'\}$ presented in the inset.

mHz⁵, over a specific period of 3.64 days. This error is derived by comparing the effective value to a representative value at the midpoint for ORF within each segment. For context and clarity in our analysis, we also depict the ORF $\Gamma_{\text{AA}'}^{\text{TL}}$, itself, along with the time-averaged ORF $\bar{\Gamma}_{\text{tot}}^{\text{TL}}$ of the TL network⁶. Our analysis reveals that as the segment duration expands from 1 hour to 4 hours, $|\mathcal{E}_r|$ rises from 0.1% to 1%. However, the period of ORF is a quarter of the period of TianQin, which is approximately

22 hours. In such a situation, if the segment duration is set to 1 hour, the contribution of the ORF (close to 0) for this small piece to the effective ORF is insignificant. Even if this portion of the data is lost, it will merely have a rather minor influence on our present analysis. Based on the above analysis, we will adopt a segment duration of 1 hour.

B. Components of stochastic background

In the mHz band, data collected by space-borne detectors has the potential to include the Galactic foreground [67, 69–71]. As the observation time extends, a growing number of individual DWDs can exceed the pre-determined detection threshold. The identification and subsequent removal of these DWDs will reduce the inten-

⁵ In our previous paper [96], it can be found that the most sensitive frequency range for the TL network is approximately between 0.5 and 5 mHz. Consequently, we utilize 1 mHz as a reference frequency.

⁶ For detailed calculations of ORF, readers can refer to our previous series of work, e.g., Refs. [71, 96, 109].

TABLE I. Coefficients for the polynomial fit for the Galactic foreground. As per the original plans for the TianQin and LISA missions, they can be scheduled for a joint operation period of up to 4 years [71]. During this operation time T , the foreground is anticipated to be depressed as the accumulated observation time grows. Note that, due to TianQin's working mode, it only offers a dataset with a duration of $T/2$ during the operation period. For example, if the operation time is 0.5 years, the duration of the dataset will be 3 months.

T	a_0	a_1	a_2	a_3	a_4	a_5	a_6
0.5 yr	-18.71	-1.41	-0.550	-2.42	2.86	10.0	-19.9
1 yr	-18.74	-1.21	-0.613	-3.07	1.89	3.15	-17.4
2 yr	-18.75	-1.47	-1.44	-0.568	2.07	-1.21	-21.1
4 yr	-18.79	-1.49	-0.895	-3.58	-8.28	1.32	-1.44

sity of the Galactic foreground. In our previous work, we established that TianQin and the LISA will be capable of simultaneous operation for up to 4 years [71]. Compared with the observation of a single detector, the joint observation of the two detectors enables more resolvable DWDs, and thus the foregrounds for TianQin and the LISA can be further depressed, respectively. Based on the two foregrounds, a joint foreground of the TL network can be derived through Eq. (41) of Ref. [71]. For the joint foreground, corresponding polynomial coefficients a_i required for Eq. (6) are specified in Table I.

In Fig. 2 (top panel), we show the energy spectrum density Ω_{gw} of the foreground using green lines. Although the foreground dominates the frequency band around mHz, its intensity sharply declines at a specific frequency. This drop frequency shifts from approximately 5 to 3 millihertz as the operation time increases, thereby revealing other backgrounds at higher frequencies that were previously masked. These exposed backgrounds can originate from the extragalactic binaries of astrophysical origin and the cosmic defects of cosmological origin [71]. For the astrophysical SGWB, the value of Ω_{ast} as defined in Eq. (7) is anticipated to fall within the range $[5.28 \times 10^{-12}, 1.32 \times 10^{-10}]$ when using a reference frequency $f_{\text{ref}} = 10 \text{ mHz}$ [71]. Regarding the cosmological SGWB, the Ω_{cos} as specified in Eq. (8) is constrained to be below 10^{-10} . As illustrated in the top panel of Fig. 2, the purple line represents the astrophysical background with $\Omega_{\text{ast}} = 2.64 \times 10^{-11}$, while the brown line denotes the cosmological background with $\Omega_{\text{cos}} = 1 \times 10^{-11}$. In the bottom panel, the PSDs of these backgrounds are illustrated, along with the 0.5-year Galactic foreground. Considering the total background, which includes these three components, we simulate 3-month data for the channel group $\{\text{A}, \text{E}, \text{A}', \text{E}'\}$ of TianQin and LISA. By cross-correlating the data from four channel pairs $\{\text{AA}', \text{AE}', \text{EA}', \text{EE}'\}$, we construct the estimator \hat{C}_{tot} as defined in Eq. (24). This estimator, along with the statistical error σ_{tot} , is also shown in the bottom

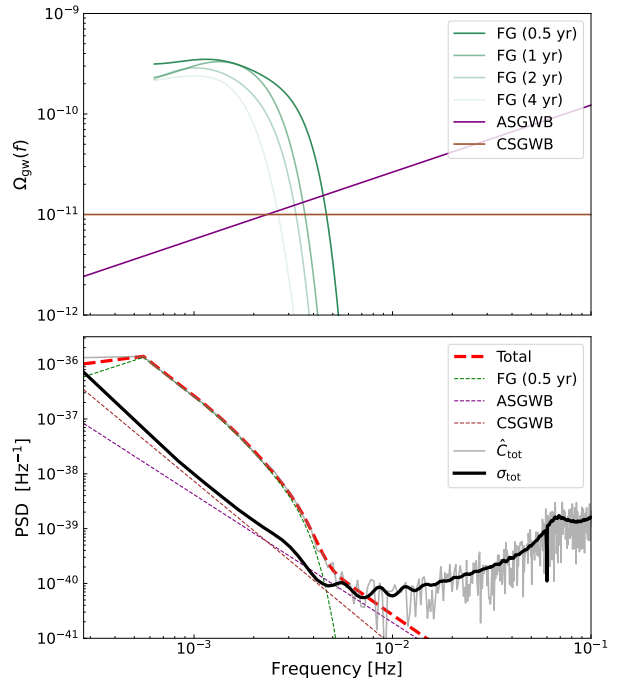


FIG. 2. Top panel: energy spectrum density of the Galactic foreground corresponding to different operation times (green), the astrophysical background (purple), and the cosmological background (brown). Bottom panel: estimator \hat{C}_{tot} (gray solid line) and standard deviation σ_{tot} (black solid line) for the 3-month simulated data of the TL network, where we approximate the total background (red dashed line) as a collection of 0.5-year Galactic foreground (green dashed line), astrophysical background (purple dashed line), and cosmological background (brown dashed line). Note that in the frequency band below 0.6 mHz, the polynomial-fitting results will plunge to 0 and no longer match the intensity of the actual Galactic foreground. Nevertheless, in this frequency band, the foreground is far lower than the detector noise. Thus, we have excluded it from the top panel. Regarding the bottom panel, to obtain the discrete data points, the Galactic foreground needs to extend to 1/3600 Hz, and two points seem to form a straight line at low frequencies.

panel. We find that the contribution of SGWBs to the estimator only surpasses that of the Galactic foreground and statistical error within the frequency range of 5 to 6 mHz. To broaden this advantageous range, it is essential to depress the Galactic foreground and statistical error by extending the operation time. It should be noted that for component separation, we only concentrate on the relative amplitude of the SGWB to the Galactic foreground. Furthermore, the peculiar long-term modulation and non-Gaussianities of the Galactic foreground can also enable component separation [74, 110–112].

C. Priors

In selecting the priors for the parameter, we opt for a weakly constrained range to ensure a robust analysis. For the Galactic foreground, the impact of higher-order polynomial coefficients a_i on its intensity becomes more pronounced. Taking into account the variations in a_i for each order across different operation times, we establish the prior ranges for these coefficients as follows:

$$a_i \in \begin{cases} [a_{i,\text{true}} - 1, a_{i,\text{true}} + 1], & i = 0, 1, 2 \\ [a_{i,\text{true}} - 5, a_{i,\text{true}} + 5], & i = 3, 4 \\ [a_{i,\text{true}} - 10, a_{i,\text{true}} + 10], & i = 5, 6 \end{cases}, \quad (31)$$

where $a_{i,\text{true}}$ represents the true value.

Regarding the other SGWB parameters, we impose uniform priors on $\log(\Omega_{\text{ast},\cos})$ and α_{ast} within a range extending two units above or below the true value, i.e., the interval $[\log(\Omega_{\text{ast},\cos}) - 2, \log(\Omega_{\text{ast},\cos}) + 2]$ and $[\alpha_{\text{ast}} - 2, \alpha_{\text{ast}} + 2]$.

D. Total PSD estimation

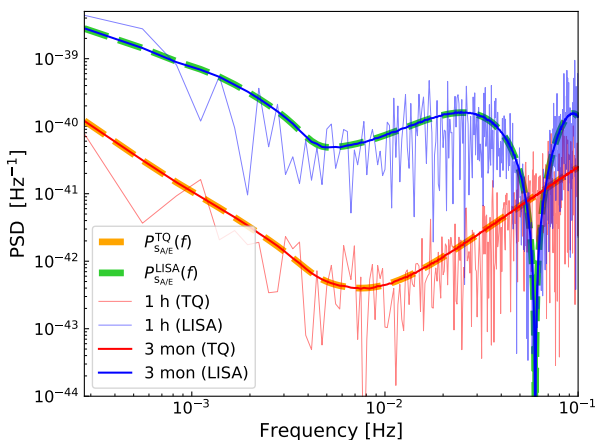


FIG. 3. Estimation of the total PSD. The thick dotted orange and green lines correspond to the true PSDs of TianQin and LISA, respectively. The solid red and blue lines depict the estimated PSDs for TianQin and LISA, derived from 1-hour and 3-month auto-correlation data.

To derive the statistical error σ_{tot} for likelihood, as shown in Eq. (26), one needs to model the total PSD P_s of the data. In this work, we estimate the total PSD by auto-correlating the data, an approach that aligns with the generation of cross-correlation data as outlined in Sec. III B. Starting from Eq. (21), the auto-correlation estimator for a given time interval can be derived by setting $I = J$ and $\Gamma_{IJ} = 1$. This estimator is inherently subject to statistical uncertainties. Nevertheless, by employing Eq. (24), which entails averaging multiple auto-

correlation data across each frequency bin, these uncertainties can be substantially reduced by a factor of $1/N$, as evidenced in Eq. (26). Assuming that the PSD is both smooth [113] and stationary⁷, a sufficiently large number of data segments N ensures that the above procedure can reliably infer the shape of the total PSD.

For the A channel of TianQin and LISA, we simulate the corresponding 3-month datasets, encompassing detector noise, Galactic foreground corresponding to an operation time of 0.5 years, and the other components of the SGWB with the energy spectrum density Ω_{gw} as depicted in Fig. 2. This dataset is subsequently divided into 2190 segments, each lasting 1 hour. As illustrated in Fig. 3, the PSD derived directly from a single 1-hour auto-correlation data segment, without the benefit of averaging, exhibits a pronounced deviation from the true PSD. In sharp contrast, averaging over all 2190 data segments dramatically reduces the statistical uncertainty, yielding an estimated PSD that is closely aligned with the true PSD. We conclude that by dividing and averaging the 3-month auto-correlation data into 1-hour segments, it is feasible to derive total PSDs, allowing us to effectively estimate the statistical error associated with the cross-correlation estimator.

V. RESULTS

In a Bayesian framework, the detection of a stochastic process is often approached through model selection. Previous studies have demonstrated that Galactic foreground can surpass the noise levels of space-borne detectors, potentially affecting the detection of other backgrounds [63–74]. Consequently, we focus on whether space-borne detectors can discern SGWBs of different origins amidst the Galactic foreground, rather than merely detecting SGWBs in the presence of pure detector noise.

In this section, we will explore the following three hypotheses: (i) \mathcal{H}_0 , which represents the sole presence of Galactic foreground; (ii) \mathcal{H}_1 , involving Galactic foreground and one additional background; and (iii) \mathcal{H}_2 , encompassing Galactic foreground and two additional backgrounds. After establishing that multi-component SGWBs can be detected and distinguished, the final step will be parameter estimation to determine the extent to which space-borne detectors can constrain the parameters of these backgrounds. It is worth emphasizing that, while the astrophysical background involves a variable index for Ω_{ast} , the cosmological background is assumed to have a fixed index of 0 for Ω_{\cos} .

Unless otherwise stated, we generate simulated datasets following the methodology outlined in Sec. III,

⁷ A more practical scenario is that a noise PSD is unable to remain stationary [114].

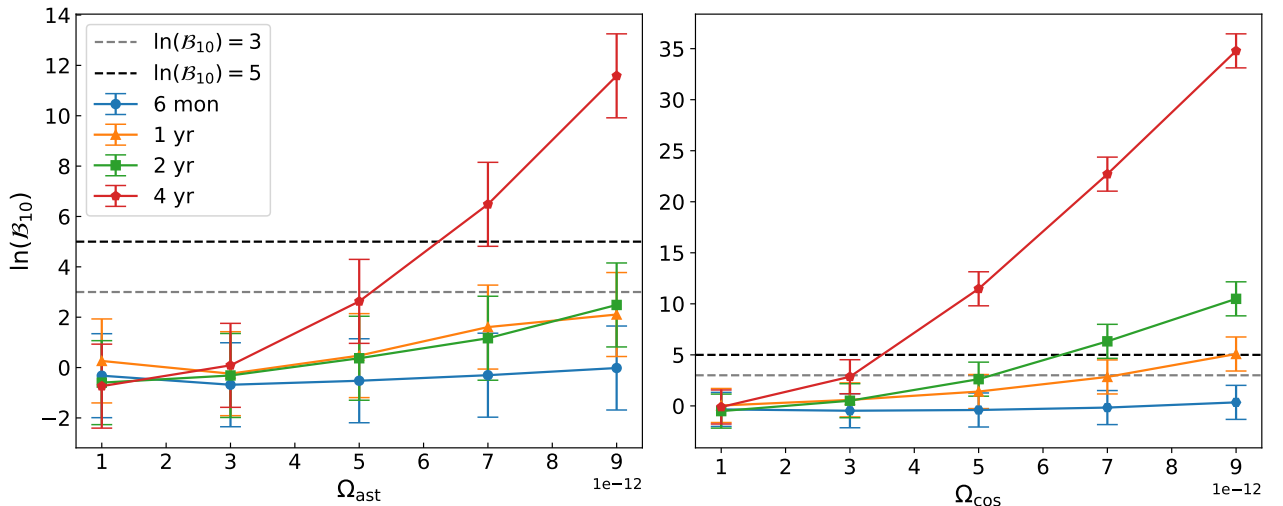


FIG. 4. Log-Bayes factor, between \mathcal{H}_0 , \mathcal{H}_1 , as a function of astrophysical energy density Ω_{ast} (with a variable index α_{ast} , left panel) and cosmological energy density Ω_{cos} (with a fixed index, right panel). The blue, orange, green, and red lines correspond to the TL network's performance over operation time of 0.5, 1, 2, and 4 years, respectively. The error bars indicate the quantiles [16%, 84%], with the points representing the median. For reference, the dashed gray lines indicate log-Bayes factors of 3 and 5, serving as thresholds for the detection of an additional SGWB in the presence of Galactic foreground.

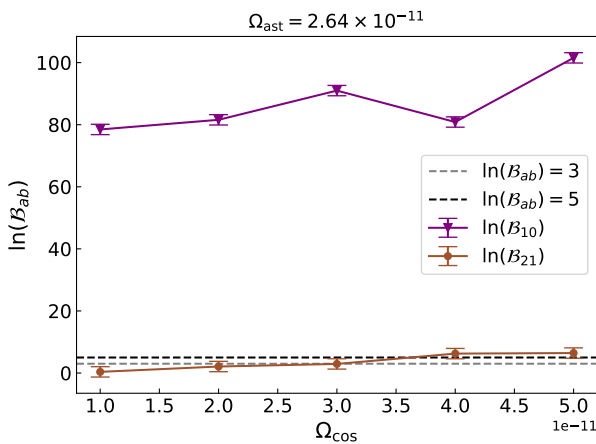


FIG. 5. Log-Bayes factors $\ln(\mathcal{B}_{10})$ (purple) and $\ln(\mathcal{B}_{21})$ (brown) for hypotheses \mathcal{H}_0 , \mathcal{H}_1 , and \mathcal{H}_2 , assuming an operation time of 4 years. The error bars indicate the quantiles [16%, 84%], with the points representing the median. The dashed gray lines represent the log-Bayes factor thresholds of 3 and 5, respectively.

utilizing the cross-correlation of the four channel pairs $\{\text{AA}', \text{AE}', \text{EA}', \text{EE}'\}$ within the TL network.

A. Model selection

We are currently engaged in calculating the log-Bayes factors across various SGWB parameters, aiming to assess the detection capability of the TL network to

SGWBs amidst the Galactic foreground. The intensity variation of the Galactic foreground over extended operation times is a key consideration in this assessment. Moving on to the astrophysical and cosmological backgrounds, we streamline the analysis by setting the astrophysical spectral index to be around 2/3 (specifically, within the range of $[1/3, 1]$)⁸. This simplification contributes to the reasonableness of the forthcoming analysis, which will be elaborated upon later.

Given the flexibility of the model, we set the energy densities $\Omega_{\text{ast/cos}}$ to be on the order of 10^{-12} , and present the log-Bayes factor between the hypotheses \mathcal{H}_0 and \mathcal{H}_1 in Fig. 4. For an astrophysical background, the $\ln \mathcal{B}_{10}$ remains below 3 even after two years of cross-correlation detection. As the operation time extends to 4 years, an astrophysical with Ω_{ast} of 7×10^{-12} can be detected, where the $\ln \mathcal{B}_{10}$ is larger than 5. Regarding a cosmological background, it can be detected with just 1 year of cross-correlation detection when the Ω_{cos} reaches 9×10^{-12} , with a $\ln \mathcal{B}_{10}$ of around 5. When the operation time extends to 4 years, the intensity threshold of Ω_{cos} can be further decreased to 5×10^{-12} , with a $\ln \mathcal{B}_{10}$ being greater than 5. Fig. 4 supports the notion that with extended operation time, the accumulation of cross-correlation data and the diminishing foreground intensity significantly boost the detection capability to other SGWBs.

The next step entails distinguishing between two back-

⁸ In this paper, we limit our focus to this simple case, rather than other complex ones, such as the background from extreme mass ratio inspirals [115–117].

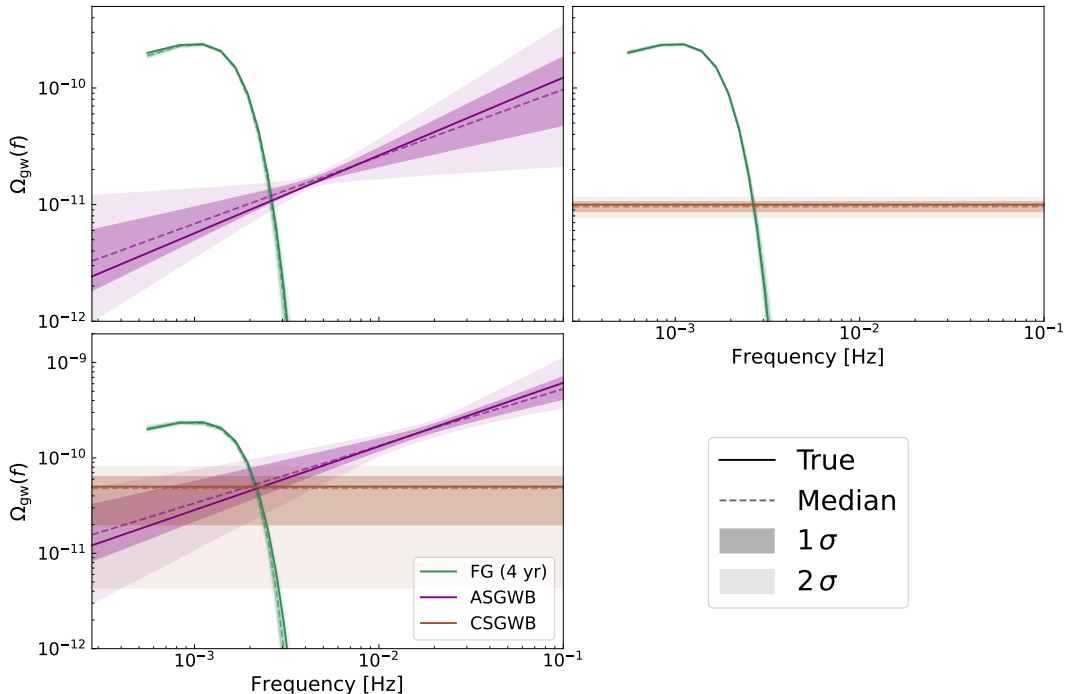


FIG. 6. Posteriors of energy spectrum densities Ω_{gw} of Galactic foreground and SGWBs, with the 4-year operation of the TL network. The green, purple, and brown lines represent the Galactic foreground, the astrophysical background, and the cosmological background, respectively. The posteriors of the Galactic foreground are related to seven polynomial coefficients a_i , those of the astrophysical background to Ω_{ast} and α_{ast} , and those of the cosmological background to Ω_{cos} . The true and estimated median values are distinguished by solid and dashed lines. The lightly shaded areas indicate the 1σ and 2σ credible regions. Both panels include a 4-year Galactic foreground: the top panel presents the parameter estimation on the astrophysical and cosmological backgrounds with $\Omega_{\text{ast}} = 2.64 \times 10^{-11}$ and $\Omega_{\text{cos}} = 1 \times 10^{-11}$, respectively; the bottom panel illustrates the parameter estimation on both the astrophysical and cosmological backgrounds, where $\Omega_{\text{ast}} = 1.32 \times 10^{-10}$ and $\Omega_{\text{cos}} = 5 \times 10^{-11}$.

grounds while the Galactic foreground is present. Detecting two backgrounds introduces new challenges compared to detecting a single one: the prior range of α_{ast} for astrophysical background can encompass the value of 0. This scenario can result in a strong cosmological background being wrongly identified as an astrophysical background. Additionally, in the model selection process, the simpler of two models that fit the data equally well is preferred [95]. Consequently, a reduced Bayesian factor between hypotheses \mathcal{H}_1 and \mathcal{H}_2 can arise. To address this issue, we have previously set the astrophysical spectral index within the range of $[1/3, 1]$. Besides, we expand the energy density $\Omega_{\text{ast/cos}}$ from 10^{-12} to 10^{-11} and set the operation time to 4 years.

Following the rules mentioned above, we employ the Galactic foreground corresponding to a 4-year operation time and set the Ω_{ast} for astrophysical background at 2.64×10^{-11} , which aligns with the median expected intensity of the extragalactic background. Furthermore, we increase the value of Ω_{cos} from 1×10^{-11} to 5×10^{-11} to demonstrate the impact of the intensity of the cosmological background on the model selection. In Fig. 5, we present the log-Bayes factor $\ln(\mathcal{B}_{21})$ between hypotheses \mathcal{H}_1 and \mathcal{H}_2 by the brown line, where the background in

\mathcal{H}_1 specifically attributed to an astrophysical origin. For comparison purposes, the purple line denotes the log-Bayes factor $\ln(\mathcal{B}_{10})$ between hypotheses \mathcal{H}_0 and \mathcal{H}_1 . With the intensities of backgrounds on the order of 10^{-11} , the 4-year data of the TL network is sufficient to provide evidence for the existence of SGWB, as $\ln(\mathcal{B}_{10}) \gg 5$. This result aligns with the results depicted in Fig. 4. Furthermore, for $\ln(\mathcal{B}_{10}) > 5$, Ω_{cos} must exceed 4×10^{-11} to enable the TL network to identify the cosmological background among the Galactic foreground and astrophysical background.

B. Parameter estimation

Having established through model selection that the 4-year operation of the TL network is capable of detecting one or more SGWBs amidst the Galactic foreground, our subsequent focus shifts to parameter estimation. This process aims to determine the precision with which the TL network can constrain the parameters of these SGWBs. Notably, in contrast to model selection, the spectral index α_{ast} now functions as a model parameter to be inferred.

We initiate the parameter estimation process for a scenario that encompasses the Galactic foreground and a single SGWB. Adhering to the parameter settings employed during model selection, we establish Ω_{ast} and Ω_{cos} to 2.64×10^{-11} and 1×10^{-11} , respectively, within a 4-year Galactic foreground. The resulting posterior distributions are illustrated in Fig. 7 and Fig. 8 of the Appendix A, where the corresponding P-P plot ensures the consistency of parameter estimation. Regarding the foreground parameter a_i , its posterior distribution widens with increasing order, indicating a growing uncertainty. The astrophysical SGWB is delineated by two parameters, Ω_{ast} and α_{ast} , which exhibit a strong correlation. This parameter correlation complicates the estimation process. In contrast, the cosmological SGWB, characterized by the single parameter Ω_{cos} , allows for a more precise constraint that closely mirrors the true value. It is noteworthy that the parameters of foreground and SGWBs do not exhibit a strong correlation. This observation justifies the use of a polynomial fit for the foreground in SGWB detection. To enhance clarity, we further consolidate the parameters of foreground and SGWBs into their spectral density parameter Ω_{gw} , with the posteriors displayed in the top panel of Fig. 6. Given that the Galactic foreground dominates near 1 mHz, its estimated median value closely matches the true value, albeit with a minor error range. Concerning the SGWBs, although the credible region is relatively expansive, the corresponding P-P plot can guarantee the consistency of parameter estimation.

In our ongoing efforts to estimate the parameters of multi-component SGWB, we adjust the Ω_{ast} of astrophysical background to the anticipated upper limit of 1.32×10^{-10} . Meanwhile, we increase the Ω_{cos} of cosmological background to 5×10^{-11} [71]. This adjustment allows us to examine the precision of our parameter estimation for the cosmological background in the presence of a foreground, particularly when the astrophysical background's intensity is at its theoretical maximum. We present the posterior distributions in Fig. 9 of the Appendix A, confirming that the true values of the corresponding ten parameters are indeed contained within the $1-\sigma$ credible intervals. We observe that when multiple components are present in the SGWB, correlations may emerge between the parameters of the different components. The resulting posteriors of energy spectrum density Ω_{gw} are illustrated in the bottom panel of Fig. 6. When compared to the detection of a single SGWB, the simultaneous detection of multiple SGWBs can lead to a loss in the precision of estimating the energy spectrum density. Nonetheless, under the model parameters chosen, the true values for both the astrophysical and cosmological backgrounds continue to lie within the $1-\sigma$ credible regions. Our findings suggest that, following 4 years of operation of the TL network, there remains a promising prospect for detecting the cosmological background within permissible models, even in the presence of a foreground and an astrophysical SGWB.

VI. SUMMARY

In this paper, we investigated the cross-correlation detection for the SGWB using a space-borne detector network. We initiated our study by deriving a tailored likelihood function specifically for scenarios involving a strong SGWB, which also enables data folding to accelerate processing. The likelihood is primarily concerned with the segment duration for data folding and the statistical error estimation of cross-correlation. Employing the TL network as a case study, we selected the segment duration to be 1 hour, taking into account the detection sensitivity band and the model error of the ORF. Meanwhile, adhering to this segmentation strategy, we employ the auto-correlation estimator to accurately estimate the statistical errors.

Building upon the established foundation, we utilized model selection and parameter estimation to forecast the detectable limits of the SGWB in the presence of the Galactic foreground. To simplify our analysis, we have assumed a fixed zero-slope for the cosmological background. Our results revealed that, by extending the operation time of the TL network from 0.5 years to 4 years, the detectable limits to the SGWB could be significantly improved. Specifically, for a single astrophysical or cosmological SGWB, an intensity of $\Omega_{\text{ast/cos}}$ on the order of 10^{-12} would be sufficient to furnish evidence of the SGWB's existence. In scenarios where both astrophysical and cosmological SGWB coexist, the Ω_{cos} should reach 2×10^{-11} to ensure the identification of the cosmological background.

For a single LISA, Boileau et al. proposed that a cosmological background energy density of approximately 8×10^{-13} could be distinguished from a Galactic foreground and the anticipated astrophysical background [76]. In contrast to our work, their work has taken into account a variable index for the cosmological background. Nevertheless, this assessment did not consider the impact of detector noise uncertainties on the null-channel method. As detailed in [46], compared to scenarios without detector noise uncertainties, the background energy density would need to be roughly 50 times higher to achieve the same measurement precision in the presence of such uncertainties. Considering this factor, the cross-correlation detection of a detector network can outperform the null-channel detection of a single detector for the SGWB.

We acknowledge the potential to expand upon our current work by delving into more complex detector noise characteristics, including non-stationary [118–123], non-Gaussian [121, 124–128], and correlated noise [129–138]. Rather than hindering the SGWB detection if modeled properly, such complexities can potentially be used to enhance the discrimination between noise and signal. Additionally, the first order phase transition (PT) with a broken power-law background can also emerge in the mHz band [139–150]. Through separating it from other backgrounds, on the one hand, the parameter estimation

of remaining backgrounds can be more precise. On the other hand, the detection of the PT background itself can also verify that the electroweak symmetry of elementary-particle physics is broken.

ACKNOWLEDGMENTS

This work has been supported by the National Key Research and Development Program of China (No. 2023YFC2206704), the National Key Research and Development Program of China (No. 2020YFC2201400), the Natural Science Foundation of China (Grants No. 12173104), and the Guangdong Basic and Applied Basic Research Foundation(Grant No. 2023A1515030116). Z.C.L. is supported by the Guangdong Basic and Applied Basic Research Foundation (Grant No. 2023A1515111184). We also thank Jian-wei Mei for the helpful discussions.

Appendix A: Results of the corner plot and P-P plot check

For comprehensive presentation, we have included the corner plots for posterior distributions of the SGWB parameters in this appendix, corresponding to the results presented in Fig. 6. Furthermore, we have conducted the corresponding P-P plots to guarantee consistency. For a completely consistent method, we anticipate that the P-P plot will follow the diagonal line with some random fluctuations. Note that, given the numerous parameters of the Galactic foreground, we present the P-P plot corresponding to the estimation of its intensity at 1 mHz.

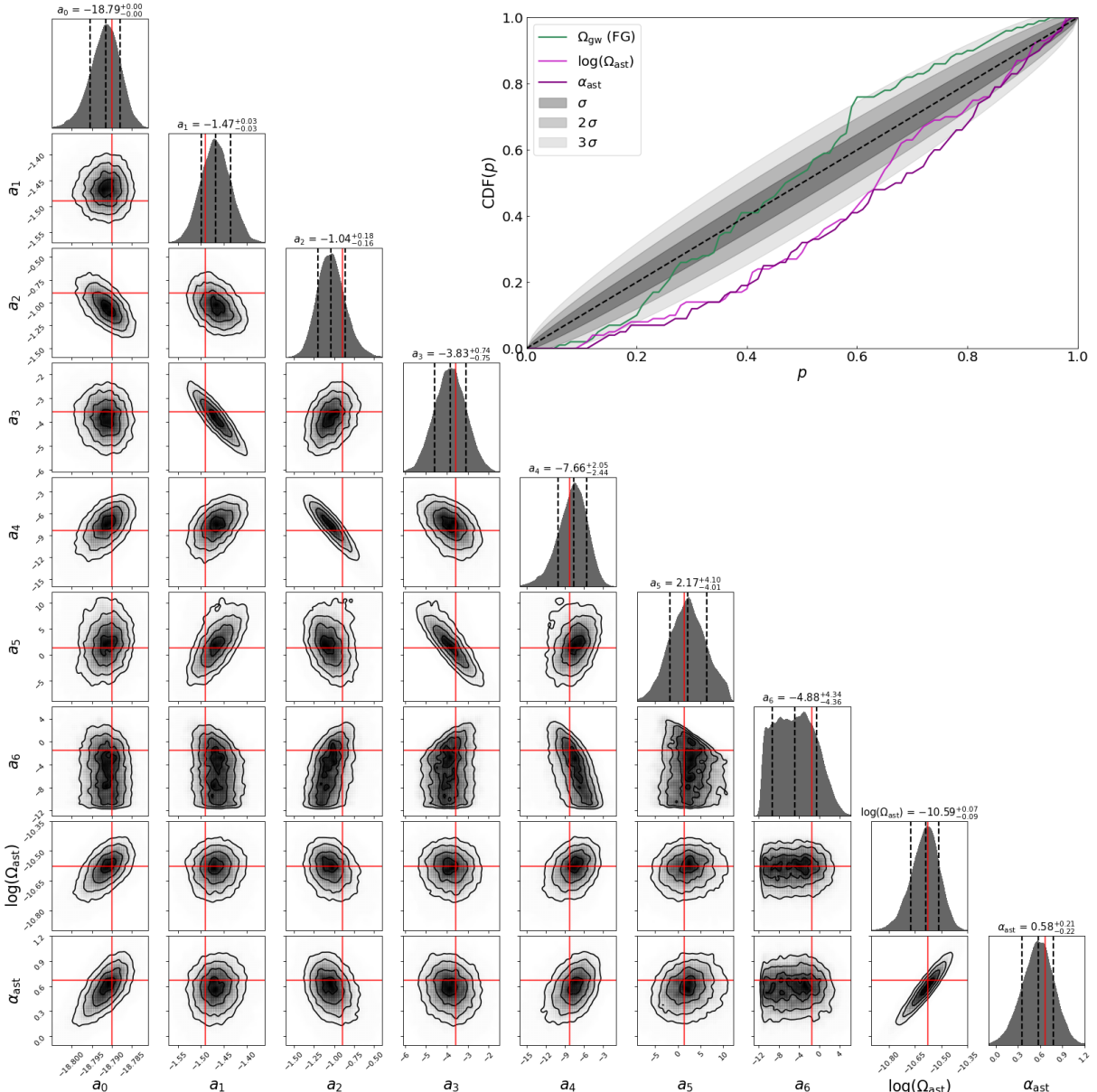


FIG. 7. Corner plot depicting the posterior distributions, generated using sampling. These results incorporate a 4-year Galactic foreground and an astrophysical background with $\Omega_{\text{ast}} = 2.64 \times 10^{-11}$. Vertical dashed lines on the posterior distributions mark the quantiles [16%, 50%, 84%], with red lines representing the true values. The inset presents the P-P plots from 100 independent simulations for estimating Ω_{gw} (green) at 1 mHz of the Galactic foreground, $\log(\Omega_{\text{ast}})$ (violet) and α_{ast} (purple) of the astrophysical background. The x -axis represents the credible level, and the y -axis represents the cumulative distribution function (CDF), which is the proportion of simulations where the true parameters lie within the credible interval. Different gray-shaded areas represent the 1- σ , 2- σ , and 3- σ confidence intervals, respectively.

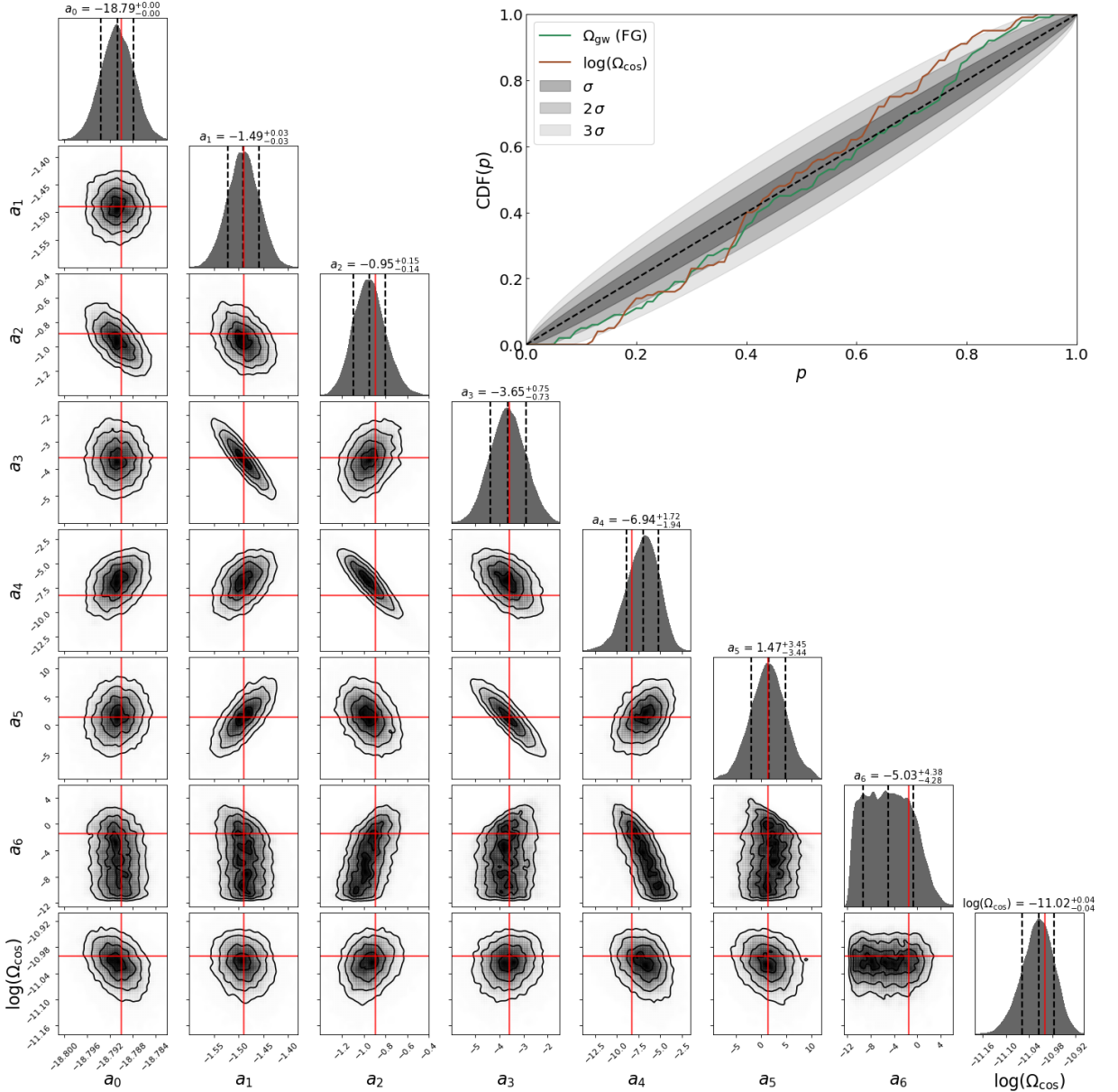


FIG. 8. Corner plot depicting the posterior distributions, generated using sampling. These results incorporate a 4-year Galactic foreground and a cosmological background with $\Omega_{\text{cos}} = 1 \times 10^{-11}$. Vertical dashed lines on the posterior distributions mark the quantiles [16%, 50%, 84%], with red lines representing the true values. The inset presents the P-P plots from 100 independent simulations for estimating Ω_{gw} (green) at 1 mHz of the Galactic foreground, $\log(\Omega_{\text{cos}})$ (brown) of the cosmological background. The x -axis represents the credible level, and the y -axis represents the CDF, which is the proportion of simulations where the true parameters lie within the credible interval. Different gray-shaded areas represent the 1- σ , 2- σ , and 3- σ confidence intervals, respectively.

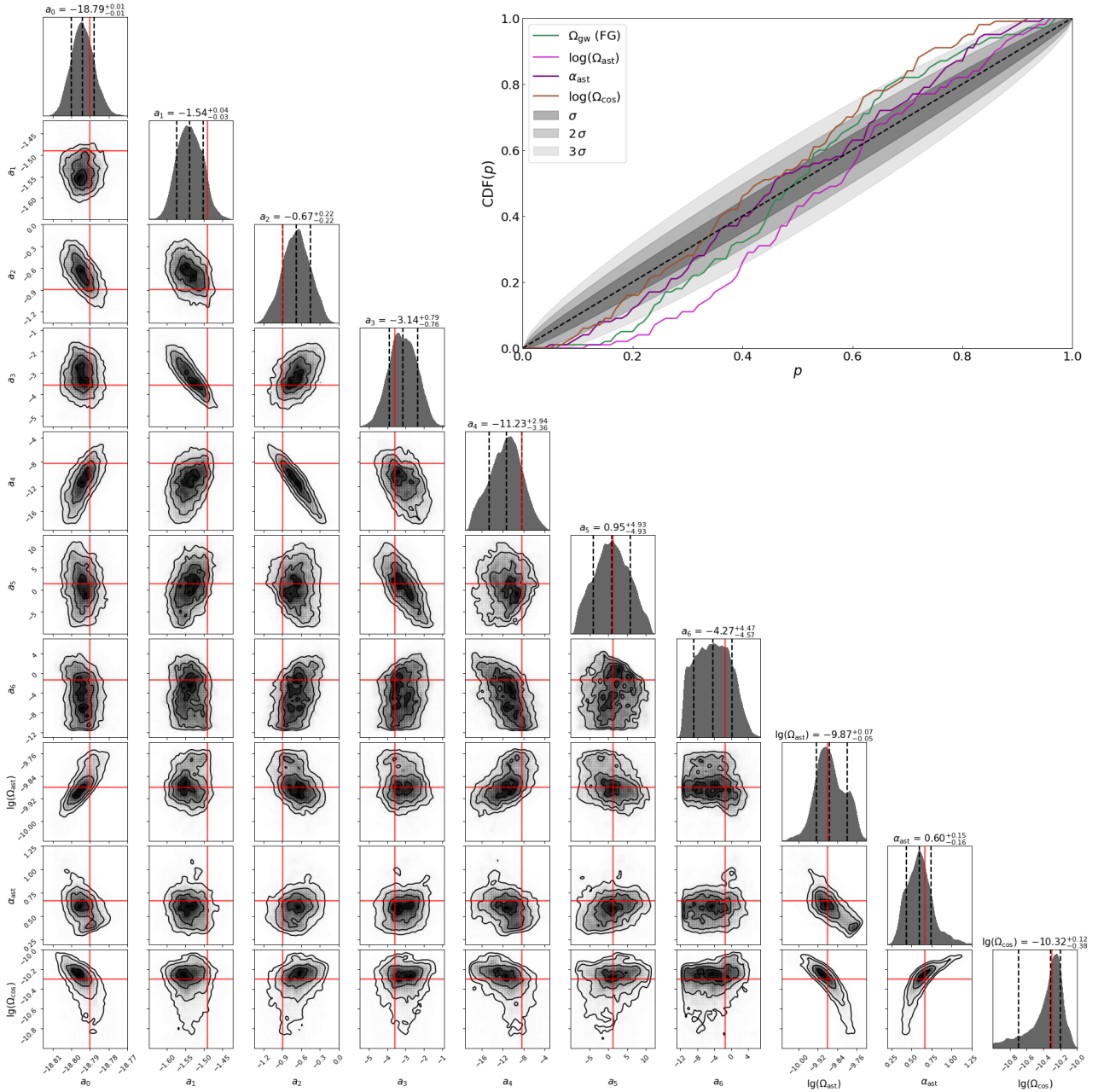


FIG. 9. Corner plot depicting the posterior distributions, generated using sampling. These results incorporate a 4-year Galactic foreground, an astrophysical background with $\Omega_{\text{ast}} = 1.32 \times 10^{-10}$, and a cosmological background with $\Omega_{\text{cos}} = 5 \times 10^{-11}$. Vertical dashed lines on the posterior distributions mark the quantiles [16%, 50%, 84%], with red lines representing the true values. The inset presents the P-P plots from 100 independent simulations for estimating Ω_{gw} (green) at 1 mHz of the Galactic foreground, $\log(\Omega_{\text{ast}})$ (violet) and α_{ast} (purple) of the astrophysical background, $\log(\Omega_{\text{cos}})$ (brown) of the cosmological background. The x -axis represents the credible level, and the y -axis represents the CDF, which is the proportion of simulations where the true parameters lie within the credible interval. Different gray-shaded areas represent the 1- σ , 2- σ , and 3- σ confidence intervals, respectively.

[2] G. Capurri, A. Lapi, C. Baccigalupi, L. Boco, G. Scelfo, and T. Ronconi, *JCAP* **11**, 032 (2021), arXiv:2103.12037 [gr-qc].

[3] N. Bellomo, D. Bertacca, A. C. Jenkins, S. Matarrese, A. Raccanelli, T. Regimbau, A. Ricciardone, and M. Sakellariadou, *JCAP* **06**, 030 (2022), arXiv:2110.15059 [gr-qc].

[4] M. Geller, A. Hook, R. Sundrum, and Y. Tsai, *Phys. Rev. Lett.* **121**, 201303 (2018), arXiv:1803.10780 [hep-ph].

[5] A. C. Jenkins and M. Sakellariadou, *Phys. Rev. D* **98**, 063509 (2018), arXiv:1802.06046 [astro-ph.CO].

[6] Y. Li, F. P. Huang, X. Wang, and X. Zhang, *Phys. Rev. D* **105**, 083527 (2022), arXiv:2112.01409 [astro-ph.CO].

[7] S. Wang, V. Vardanyan, and K. Kohri, *Phys. Rev. D* **106**, 123511 (2022), arXiv:2107.01935 [gr-qc].

[8] S. Profumo and F. Yang, *Phys. Rev. D* **108**, 103528 (2023), arXiv:2306.07454 [astro-ph.CO].

[9] F. Schulze, L. Valbusa Dall'Armi, J. Lesgourgues, A. Ricciardone, N. Bartolo, D. Bertacca, C. Fidler, and S. Matarrese, *JCAP* **10**, 025 (2023), arXiv:2305.01602 [gr-qc].

[10] S. Jiang, F. P. Huang, and P. Ko, *JHEP* **07**, 053 (2024), arXiv:2404.16509 [hep-ph].

[11] R. Hellings and G. Downs, *Astrophys. J. Lett.* **265**, L39 (1983).

[12] P. F. Michelson, *Monthly Notices of the Royal Astronomical Society* **227**, 933 (1987).

[13] N. Christensen, *Phys. Rev. D* **46**, 5250 (1992).

[14] E. E. Flanagan, *Phys. Rev. D* **48**, 2389 (1993), arXiv:astro-ph/9305029 [astro-ph].

[15] B. Allen and J. D. Romano, *Phys. Rev. D* **59**, 102001 (1999), arXiv:gr-qc/9710117 [gr-qc].

[16] C. Ungarelli and A. Vecchio, *Phys. Rev. D* **64**, 121501 (2001), arXiv:astro-ph/0106538.

[17] B. P. Abbott *et al.* (LIGO Scientific, Virgo), *Phys. Rev. Lett.* **120**, 091101 (2018), arXiv:1710.05837 [gr-qc].

[18] Y. Hu, P.-P. Wang, Y.-J. Tan, and C.-G. Shao, *Astrophys. J.* **961**, 116 (2024).

[19] M. Tinto, J. W. Armstrong, and F. B. Estabrook, *Phys. Rev. D* **63**, 021101 (2001).

[20] C. J. Hogan and P. L. Bender, *Phys. Rev. D* **64**, 062002 (2001), arXiv:astro-ph/0104266.

[21] T. L. Smith and R. Caldwell, *Phys. Rev. D* **100**, 104055 (2019), arXiv:1908.00546 [astro-ph.CO].

[22] M. Muratore, D. Vetrugno, S. Vitale, and O. Hartwig, *Phys. Rev. D* **105**, 023009 (2022), arXiv:2108.02738 [gr-qc].

[23] B. P. Abbott *et al.* (LIGO Scientific, VIRGO), *Nature* **460**, 990 (2009), arXiv:0910.5772 [astro-ph.CO].

[24] J. Abadie *et al.* (LIGO Scientific, VIRGO), *Phys. Rev. D* **85**, 122001 (2012), arXiv:1112.5004 [gr-qc].

[25] J. Aasi *et al.* (LIGO Scientific, VIRGO), *Phys. Rev. Lett.* **113**, 231101 (2014), arXiv:1406.4556 [gr-qc].

[26] B. P. Abbott *et al.* (LIGO Scientific, Virgo), *Phys. Rev. Lett.* **118**, 121101 (2017), [Erratum: *Phys. Rev. Lett.* **119**, 029901 (2017)], arXiv:1612.02029 [gr-qc].

[27] B. P. Abbott *et al.* (LIGO Scientific, Virgo), *Phys. Rev. D* **100**, 061101 (2019), arXiv:1903.02886 [gr-qc].

[28] R. Abbott *et al.* (KAGRA, Virgo, LIGO Scientific), *Phys. Rev. D* **104**, 022005 (2021), arXiv:2103.08520 [gr-qc].

[29] F. De Lillo and J. Suresh, *Phys. Rev. D* **109**, 103013 (2024), arXiv:2310.05823 [gr-qc].

[30] G. Agazie *et al.* (NANOGrav), *Astrophys. J. Lett.* **951**, L8 (2023), arXiv:2306.16213 [astro-ph.HE].

[31] H. Xu *et al.*, *Res. Astron. Astrophys.* **23**, 075024 (2023), arXiv:2306.16216 [astro-ph.HE].

[32] J. Antoniadis *et al.* (EPTA, InPTA:), *Astron. Astrophys.* **678**, A50 (2023), arXiv:2306.16214 [astro-ph.HE].

[33] D. J. Reardon *et al.*, *Astrophys. J. Lett.* **951**, L6 (2023), arXiv:2306.16215 [astro-ph.HE].

[34] M. R. Adams and N. J. Cornish, *Phys. Rev. D* **82**, 022002 (2010), arXiv:1002.1291 [gr-qc].

[35] M. R. Adams and N. J. Cornish, *Phys. Rev. D* **89**, 022001 (2014), arXiv:1307.4116 [gr-qc].

[36] C. Caprini, D. G. Figueira, R. Flauger, G. Nardini, M. Peloso, M. Pieroni, A. Ricciardone, and G. Tasinato, *JCAP* **11**, 017 (2019), arXiv:1906.09244 [astro-ph.CO].

[37] G. Boileau, N. Christensen, R. Meyer, and N. J. Cornish, *Phys. Rev. D* **103**, 103529 (2021), arXiv:2011.05055 [gr-qc].

[38] R. Flauger, N. Karsenis, G. Nardini, M. Pieroni, A. Ricciardone, and J. Torrado, *JCAP* **01**, 059 (2021), arXiv:2009.11845 [astro-ph.CO].

[39] S. Banagiri, A. Criswell, T. Kuan, V. Mandic, J. D. Romano, and S. R. Taylor, *Mon. Not. Roy. Astron. Soc.* **507**, 5451 (2021), arXiv:2103.00826 [astro-ph.IM].

[40] J. Cheng, E.-K. Li, Y.-M. Hu, Z.-C. Liang, J.-d. Zhang, and J. Mei, *Phys. Rev. D* **106**, 124027 (2022), arXiv:2208.11615 [gr-qc].

[41] G. Boileau, N. Christensen, C. Gowling, M. Hindmarsh, and R. Meyer, *JCAP* **02**, 056 (2023), arXiv:2209.13277 [gr-qc].

[42] C. Gowling, M. Hindmarsh, D. C. Hooper, and J. Torrado, *JCAP* **04**, 061 (2023), arXiv:2209.13551 [astro-ph.CO].

[43] Q. Baghi, N. Karsenis, J.-B. Bayle, M. Besançon, and H. Inchauspé, *JCAP* **04**, 066 (2023), arXiv:2302.12573 [gr-qc].

[44] G. Wang, B. Li, P. Xu, and X. Fan, *Phys. Rev. D* **106**, 044054 (2022), arXiv:2201.10902 [gr-qc].

[45] O. Hartwig, M. Lilley, M. Muratore, and M. Pieroni, *Phys. Rev. D* **107**, 123531 (2023), arXiv:2303.15929 [gr-qc].

[46] M. Muratore, J. Gair, and L. Speri, *Phys. Rev. D* **109**, 042001 (2024), arXiv:2308.01056 [gr-qc].

[47] J. Alvey, U. Bhardwaj, V. Domcke, M. Pieroni, and C. Weniger, *Phys. Rev. D* **109**, 083008 (2024), arXiv:2309.07954 [gr-qc].

[48] F. Pozzoli, R. Buscicchio, C. J. Moore, F. Haardt, and A. Sesana, *Phys. Rev. D* **109**, 083029 (2024), arXiv:2311.12111 [astro-ph.CO].

[49] A. Parida, S. Mitra, and S. Jhingan, *JCAP* **04**, 024 (2016), arXiv:1510.07994 [astro-ph.CO].

[50] S. Sachdev, T. Regimbau, and B. S. Sathyaprakash, *Phys. Rev. D* **102**, 024051 (2020), arXiv:2002.05365 [gr-qc].

[51] S. Biscoveanu, C. Talbot, E. Thrane, and R. Smith, *Phys. Rev. Lett.* **125**, 241101 (2020), arXiv:2009.04418 [astro-ph.HE].

[52] K. Martinovic, P. M. Meyers, M. Sakellariadou, and N. Christensen, *Phys. Rev. D* **103**, 043023 (2021), arXiv:2011.05697 [gr-qc].

[53] A. Sharma and J. Harms, *Phys. Rev. D* **102**, 063009 (2020), arXiv:2006.16116 [gr-qc].

[54] D. Poletti, *JCAP* **05**, 052 (2021), arXiv:2101.02713 [gr-qc].

[55] A. R. Kaiser, N. S. Pol, M. A. McLaughlin, S. Chen, J. S. Hazboun, L. Z. Kelley, J. Simon, S. R. Taylor, S. J. Vigeland, and C. A. Witt, *Astrophys. J.* **938**, 115 (2022), arXiv:2208.02307 [astro-ph.CO].

[56] B. Zhou, L. Reali, E. Berti, M. Çalışkan, C. Creque-Sarbinowski, M. Kamionkowski, and B. S. Sathyaprakash, *Phys. Rev. D* **108**, 064040 (2023), arXiv:2209.01310 [gr-qc].

[57] D. Racco and D. Poletti, *JCAP* **04**, 054 (2023), arXiv:2212.06602 [astro-ph.CO].

[58] Z. Pan and H. Yang, *Phys. Rev. D* **107**, 123036 (2023), arXiv:2301.04529 [gr-qc].

[59] D. S. Bellie, S. Banagiri, Z. Doctor, and V. Kalogera, (2023), arXiv:2310.02517 [gr-qc].

[60] H. Song, D. Liang, Z. Wang, and L. Shao, (2024), arXiv:2401.00984 [gr-qc].

[61] H. Zhong, B. Zhou, L. Reali, E. Berti, and V. Mandic, (2024), arXiv:2406.10757 [gr-qc].

[62] R. Niu and W. Zhao, (2024), arXiv:2406.12789 [gr-qc].

[63] P. L. Bender and D. Hils, *Class. Quant. Grav.* **14**, 1439 (1997).

[64] G. Nelemans, L. R. Yungelson, and S. F. Portegies Zwart, *Astron. Astrophys.* **375**, 890 (2001), arXiv:astro-ph/0105221.

[65] L. Barack and C. Cutler, *Phys. Rev. D* **70**, 122002 (2004), arXiv:gr-qc/0409010.

[66] J. A. Edlund, M. Tinto, A. Krolak, and G. Nelemans, *Phys. Rev. D* **71**, 122003 (2005), arXiv:gr-qc/0504112.

[67] A. J. Ruiter, K. Belczynski, M. Benacquista, S. L. Larson, and G. Williams, *Astrophys. J.* **717**, 1006 (2010), arXiv:0705.3272 [astro-ph].

[68] G. Nelemans, *Class. Quant. Grav.* **26**, 094030 (2009), arXiv:0901.1778 [astro-ph.SR].

[69] N. Cornish and T. Robson, *J. Phys. Conf. Ser.* **840**, 012024 (2017), arXiv:1703.09858 [astro-ph.IM].

[70] S.-J. Huang, Y.-M. Hu, V. Korol, P.-C. Li, Z.-C. Liang, Y. Lu, H.-T. Wang, S. Yu, and J. Mei, *Phys. Rev. D* **102**, 063021 (2020), arXiv:2005.07889 [astro-ph.HE].

[71] Z.-C. Liang, Y.-M. Hu, Y. Jiang, J. Cheng, J.-d. Zhang, and J. Mei, *Phys. Rev. D* **105**, 022001 (2022), arXiv:2107.08643 [astro-ph.CO].

[72] S. Staelens and G. Nelemans, *Astron. Astrophys.* **683**, A139 (2024), arXiv:2310.19448 [astro-ph.HE].

[73] S. Hofman and G. Nelemans, (2024), arXiv:2407.10642 [astro-ph.HE].

[74] F. Pozzoli, R. Buscicchio, A. Klein, V. Korol, A. Sesana, and F. Haardt, (2024), arXiv:2410.08274 [astro-ph.GA].

[75] M. Hindmarsh, D. C. Hooper, T. Minkkinen, and D. J. Weir, (2024), arXiv:2406.04894 [astro-ph.CO].

[76] G. Boileau, A. Lamberts, N. J. Cornish, and R. Meyer, *Mon. Not. Roy. Astron. Soc.* **508**, 803 (2021), [Erratum: Mon.Not.Roy.Astron.Soc. 508, 5554–5555 (2021)], arXiv:2105.04283 [gr-qc].

[77] J. Skilling, *Bayesian Analysis* **1**, 833 (2006).

[78] E. Higson, W. Handley, M. Hobson, and A. Lasenby, *Mon. Not. Roy. Astron. Soc.* **483**, 2044 (2019), arXiv:1804.06406 [stat.CO].

[79] J. S. Speagle, *Mon. Not. Roy. Astron. Soc.* **493**, 3132 (2020), arXiv:1904.02180 [astro-ph.IM].

[80] G. Ashton *et al.*, *Nature* **2** (2022), 10.1038/s43586-022-00121-x, arXiv:2205.15570 [stat.CO].

[81] E.-K. Li *et al.*, (2024), arXiv:2409.19665 [astro-ph.GA].

[82] M. Colpi *et al.*, (2024), arXiv:2402.07571 [astro-ph.CO].

[83] A. Ain, P. Dalvi, and S. Mitra, *Phys. Rev. D* **92**, 022003 (2015), arXiv:1504.01714 [gr-qc].

[84] A. Ain, J. Suresh, and S. Mitra, *Phys. Rev. D* **98**, 024001 (2018), arXiv:1803.08285 [gr-qc].

[85] C. W. Misner, K. S. Thorne, and J. A. Wheeler, *Gravitation* (W. H. Freeman, San Francisco, 1973).

[86] B. Allen, in *Les Houches School of Physics: Astrophysical Sources of Gravitational Radiation* (1996) pp. 373–417, arXiv:gr-qc/9604033.

[87] E. Thrane and J. D. Romano, *Phys. Rev. D* **88**, 124032 (2013), arXiv:1310.5300 [astro-ph.IM].

[88] Z.-C. Liang, Z.-Y. Li, E.-K. Li, J.-d. Zhang, and Y.-M. Hu, *Results Phys.* **63**, 107876 (2024), arXiv:2403.18709 [gr-qc].

[89] N. J. Cornish and S. L. Larson, *Class. Quant. Grav.* **18**, 3473 (2001), arXiv:gr-qc/0103075.

[90] E. S. Phinney, (2001), arXiv:astro-ph/0108028.

[91] D. G. Figueiroa, M. Hindmarsh, and J. Urrestilla, *Phys. Rev. Lett.* **110**, 101302 (2013), arXiv:1212.5458 [astro-ph.CO].

[92] M. Maggiore, *Gravitational Waves. Vol. 2: Astrophysics and Cosmology* (Oxford University Press, 2018).

[93] P. Auclair *et al.*, *JCAP* **04**, 034 (2020), arXiv:1909.00819 [astro-ph.CO].

[94] J. Luo *et al.* (TianQin), *Class. Quant. Grav.* **33**, 035010 (2016), arXiv:1512.02076 [astro-ph.IM].

[95] J. D. Romano and N. J. Cornish, *Living Rev. Rel.* **20**, 2 (2017), arXiv:1608.06889 [gr-qc].

[96] Z.-C. Liang, Z.-Y. Li, J. Cheng, E.-K. Li, J.-d. Zhang, and Y.-M. Hu, *Phys. Rev. D* **107**, 083033 (2023), arXiv:2212.02852 [astro-ph.GA].

[97] M. Tinto and J. W. Armstrong, *Phys. Rev. D* **59**, 102003 (1999).

[98] M. Tinto and S. V. Dhurandhar, *Living Rev. Rel.* **24**, 1 (2021).

[99] M. Vallisneri, J. Crowder, and M. Tinto, *Class. Quant. Grav.* **25**, 065005 (2008), arXiv:0710.4369 [gr-qc].

[100] J. Mei *et al.* (TianQin), (2020), 10.1093/ptep/ptaa114, arXiv:2008.10332 [gr-qc].

[101] S. Babak, A. Petiteau, and M. Hewitson, (2021), arXiv:2108.01167 [astro-ph.IM].

[102] R. E. Kass and A. E. Raftery, *Journal of the American Statistical Association* **90**, 773 (1995).

[103] <https://github.com/joshspeagle/dynesty>.

[104] J. Aasi *et al.* (LIGO Scientific, VIRGO), *Phys. Rev. D* **91**, 022003 (2015), arXiv:1410.6211 [gr-qc].

[105] N. Seto, *Phys. Rev. D* **102**, 123547 (2020), arXiv:2010.06877 [gr-qc].

[106] T. Callister, L. Sammut, S. Qiu, I. Mandel, and E. Thrane, *Phys. Rev. X* **6**, 031018 (2016), arXiv:1604.02513 [gr-qc].

[107] T. Callister, A. S. Biscoveanu, N. Christensen, M. Isi, A. Matas, O. Minazzoli, T. Regimbau, M. Sakellariadou, J. Tasson, and E. Thrane, *Phys. Rev. X* **7**, 041058 (2017), arXiv:1704.08373 [gr-qc].

[108] Y. Hu, P.-P. Wang, Y.-J. Tan, and C.-G. Shao, *Phys. Rev. D* **107**, 024026 (2023).

[109] Z.-C. Liang, Z.-Y. Li, E.-K. Li, J.-d. Zhang, and Y.-M. Hu, *Phys. Rev. D* **110**, 043031 (2024), arXiv:2307.01541 [gr-qc].

[110] R. Buscicchio, A. Klein, V. Korol, F. Di Renzo, C. J. Moore, D. Gerosa, and A. Carzaniga, (2024), arXiv:2410.08263 [astro-ph.HE].

[111] N. Karnesis, A. Sasli, R. Buscicchio, and N. Stergioulas, (2024), arXiv:2410.14354 [gr-qc].

[112] R. Rosati and T. B. Littenberg, (2024), arXiv:2410.17180 [gr-qc].

[113] P. Welch, *IEEE Transactions on Audio and Electroacoustics* **15**, 70 (1967).

[114] M. Armano *et al.* (LISA Pathfinder), *Phys. Rev. D* **110**, 042004 (2024), arXiv:2405.05207 [astro-ph.IM].

[115] M. Bonetti and A. Sesana, *Phys. Rev. D* **102**, 103023 (2020), arXiv:2007.14403 [astro-ph.GA].

[116] F. Pozzoli, S. Babak, A. Sesana, M. Bonetti, and N. Karnesis, *Phys. Rev. D* **108**, 103039 (2023), [Erratum: *Phys. Rev. D* 110, 049903 (2024)], arXiv:2302.07043 [astro-ph.GA].

[117] M. Piarulli, R. Buscicchio, F. Pozzoli, O. Burke, M. Bonetti, and A. Sesana, (2024), arXiv:2410.08862 [astro-ph.HE].

[118] N. J. Cornish and T. B. Littenberg, *Class. Quant. Grav.* **32**, 135012 (2015), arXiv:1410.3835 [gr-qc].

[119] J. Powell, *Class. Quant. Grav.* **35**, 155017 (2018), arXiv:1803.11346 [astro-ph.IM].

[120] T. Robson and N. J. Cornish, *Phys. Rev. D* **99**, 024019 (2019), arXiv:1811.04490 [gr-qc].

[121] B. Zackay, T. Venumadhav, J. Roulet, L. Dai, and M. Zaldarriaga, *Phys. Rev. D* **104**, 063034 (2021), arXiv:1908.05644 [astro-ph.IM].

[122] D. Davis, T. B. Littenberg, I. M. Romero-Shaw, M. Millhouse, J. McIver, F. Di Renzo, and G. Ashton, *Class. Quant. Grav.* **39**, 245013 (2022), arXiv:2207.03429 [astro-ph.IM].

[123] S. Kumar, A. H. Nitz, and X. J. Forteza, (2022), arXiv:2202.12762 [astro-ph.IM].

[124] B. Allen, J. D. E. Creighton, E. E. Flanagan, and J. D. Romano, *Phys. Rev. D* **65**, 122002 (2002), arXiv:gr-qc/0105100.

[125] B. Allen, J. D. E. Creighton, E. E. Flanagan, and J. D. Romano, *Phys. Rev. D* **67**, 122002 (2003), arXiv:gr-qc/0205015.

[126] Y. Himemoto, A. Taruya, H. Kudoh, and T. Hiramatsu, *Phys. Rev. D* **75**, 022003 (2007), arXiv:gr-qc/0607015.

[127] L. Martellini and T. Regimbau, *Phys. Rev. D* **92**, 104025 (2015), [Erratum: *Phys. Rev. D* 97, 049903 (2018)], arXiv:1509.04802 [astro-ph.CO].

[128] T. Yamamoto, K. Hayama, S. Mano, Y. Itoh, and N. Kanda, *Phys. Rev. D* **93**, 082005 (2016).

[129] E. Thrane, N. Christensen, and R. Schofield, *Phys. Rev. D* **87**, 123009 (2013), arXiv:1303.2613 [astro-ph.IM].

[130] E. Thrane, N. Christensen, R. M. S. Schofield, and A. Effler, *Phys. Rev. D* **90**, 023013 (2014), arXiv:1406.2367 [astro-ph.IM].

[131] M. W. Coughlin *et al.*, *Class. Quant. Grav.* **33**, 224003 (2016), arXiv:1606.01011 [gr-qc].

[132] I. Kowalska-Leszczyńska *et al.*, *Class. Quant. Grav.* **34**, 074002 (2017), arXiv:1612.01102 [astro-ph.IM].

[133] Y. Himemoto and A. Taruya, *Phys. Rev. D* **96**, 022004 (2017), arXiv:1704.07084 [astro-ph.IM].

[134] P. M. Meyers, K. Martinovic, N. Christensen, and M. Sakellariadou, *Phys. Rev. D* **102**, 102005 (2020), arXiv:2008.00789 [gr-qc].

[135] K. Janssens, K. Martinovic, N. Christensen, P. M. Meyers, and M. Sakellariadou, *Phys. Rev. D* **104**, 122006 (2021), [Erratum: *Phys. Rev. D* 105, 109904 (2022)], arXiv:2110.14730 [gr-qc].

[136] K. Janssens, T. A. Callister, N. Christensen, M. W. Coughlin, I. Michaloliakos, J. Suresh, and N. van Remortel, *Phys. Rev. D* **105**, 082001 (2022), arXiv:2112.03560 [gr-qc].

[137] Y. Himemoto, A. Nishizawa, and A. Taruya, *Phys. Rev. D* **107**, 064055 (2023), arXiv:2302.03336 [gr-qc].

[138] K. Janssens *et al.*, *Phys. Rev. D* **109**, 102002 (2024), arXiv:2402.17320 [gr-qc].

[139] C. Caprini, R. Durrer, and G. Servant, *JCAP* **12**, 024 (2009), arXiv:0909.0622 [astro-ph.CO].

[140] M. Hindmarsh, S. J. Huber, K. Rummukainen, and D. J. Weir, *Phys. Rev. Lett.* **112**, 041301 (2014), arXiv:1304.2433 [hep-ph].

[141] R. Jinno and M. Takimoto, *Phys. Rev. D* **95**, 024009 (2017), arXiv:1605.01403 [astro-ph.CO].

[142] R. Jinno and M. Takimoto, *JCAP* **01**, 060 (2019), arXiv:1707.03111 [hep-ph].

[143] M. Hindmarsh, S. J. Huber, K. Rummukainen, and D. J. Weir, *Phys. Rev. D* **96**, 103520 (2017), [Erratum: *Phys. Rev. D* 101, 089902 (2020)], arXiv:1704.05871 [astro-ph.CO].

[144] D. Cutting, M. Hindmarsh, and D. J. Weir, *Phys. Rev. D* **97**, 123513 (2018), arXiv:1802.05712 [astro-ph.CO].

[145] F. P. Huang and X. Zhang, *Phys. Lett. B* **788**, 288 (2019), arXiv:1701.04338 [hep-ph].

[146] A. Mazumdar and G. White, *Rept. Prog. Phys.* **82**, 076901 (2019), arXiv:1811.01948 [hep-ph].

[147] X. Wang, F. P. Huang, and X. Zhang, *JCAP* **05**, 045 (2020), arXiv:2003.08892 [hep-ph].

[148] Y. Di, J. Wang, R. Zhou, L. Bian, R.-G. Cai, and J. Liu, *Phys. Rev. Lett.* **126**, 251102 (2021), arXiv:2012.15625 [astro-ph.CO].

[149] X. Wang, F. P. Huang, and Y. Li, *Phys. Rev. D* **105**, 103513 (2022), arXiv:2112.14650 [astro-ph.CO].

[150] S. Jiang, F. P. Huang, and C. S. Li, *Phys. Rev. D* **108**, 063508 (2023), arXiv:2305.02218 [hep-ph].